processes

MDPI

Article

Study on the Imbibition Law of Laminated Shale Oil Reservoir During Injection and Shut-In Period Based on Phase Field Method

Kun Yang [1], Shenglai Yang [1,*], Xinyue Liu [1], Shuai Zhao [1] and Jilun Kang [2]

[1] National Key Laboratory of Petroleum Resources and Engineering, China University of Petroleum (Beijing), Beijing 102249, China; yangkun_cup@163.com (K.Y.); liuxy_cup@163.com (X.L.); shuaizhao0726@163.com (S.Z.)
[2] Research Institute of Exploration and Development, Tuha Oilfield Company, Petro China, Hami 839009, China; kang_jilun123@163.com
* Correspondence: yangsl@cup.edu.cn

Abstract: Laminated shale oil reservoirs feature well-developed microcracks, with significant differences in wettability on either side of these fractures. The complex pore structure of laminated shale oil reservoirs makes capillary imbibition prevalent during both water injection and well shut-in periods. Therefore, based on the phase field method, this study investigates the imbibition behavior and the influencing factors during the injection and shut-in stage. This research shows that the imbibition mode determines the recovery rate: co-current imbibition > co-current imbibition + counter-current imbibition > counter-current imbibition. Co-current imbibition predominantly occurs in the dominant seepage channels, while counter-current imbibition mainly takes place in pore boundary regions. During the water injection stage, a low injection rate is beneficial for synergistic oil recovery through imbibition and displacement. As the injection rate increases, the capillary imbibition effect diminishes. Increased water saturation strengthens the co-current imbibition effect. Compared to injecting for 5 ms, injecting for 10 ms resulted in a 4.53% increase in imbibition recovery during the shut-in stage. The water sweep efficiency increases with the tortuosity of fractures. The wettability differences on either side of the fractures have a certain impact on imbibition. Around the fracture, the recovery in the strongly wetted area is 35% higher than that in the weakly water-wetted area. The wettability difference across fractures causes water to penetrate along the strongly water-wet pores, while only the inlet end and the pores near the fracture in the weakly water-wet zone are affected. Therefore, it is crucial to monitor the injection pressure to maximize the synergistic effects of displacement and imbibition during the development of laminated shale oil reservoirs. Additionally, surfactants should be used judiciously to prevent fingering due to wettability differences.

Keywords: imbibition; fracture; wettability; tortuosity; shale oil

check for updates

Academic Editors: Jan Vinogradov and Ali Habibi

Received: 9 January 2025
Revised: 6 February 2025
Accepted: 8 February 2025
Published: 10 February 2025

Citation: Yang, K.; Yang, S.; Liu, X.; Zhao, S.; Kang, J. Study on the Imbibition Law of Laminated Shale Oil Reservoir During Injection and Shut-In Period Based on Phase Field Method. *Processes* **2025**, *13*, 481. https://doi.org/10.3390/pr13020481

Copyright: © 2025 by the authors. Licensee MDPI, Basel, Switzerland. This article is an open access article distributed under the terms and conditions of the Creative Commons Attribution (CC BY) license (https://creativecommons.org/licenses/by/4.0/).

1. Introduction

China possesses abundant shale oil resources, and the development of these resources has garnered significant attention, particularly with the application of horizontal well technology and volume pressure techniques [1,2]. Nonetheless, the shale oil recovery rate remains limited because of the extremely low porosity and permeability, as well as the intricate pore-throat structures inherent to shale oil reservoirs [3,4]. The fracture network created through horizontal well fracturing enhances the contact area between the water and the rock matrix. Additionally, the numerous micro-nano pores within the matrix amplify the capillary forces present in the reservoir. Consequently, the imbibition effect,

driven by capillary forces, significantly impacts the recovery rate in shale oil reservoirs [5,6]. Imbibition can occur during various stages of well operations, including drilling, fracturing, and well shut-in [7,8].

To better understand the principles of imbibition during oil reservoir production, researchers have conducted extensive studies [9–11]. Employing the Lucas–Washburn equation in conjunction with Handy's model [12], scholars have formulated a diverse array of imbibition models [13,14]. Through core experiments [15–17], researchers have conducted comprehensive investigations into the imbibition mechanisms. The critical factors governing imbibition efficiency have been identified as rock wettability, oil–water interfacial tension, and pore-throat microstructure of cores [18,19]. Cai et al. [20] proposed an imbibition fractal model based on the LW model and constructed a bond number fractal model to study the factors influencing imbibition. Wang et al. [21] studied the factors affecting imbibition through imbibition experiments and mechanism models. The results showed that enhancing wettability can improve imbibition recovery. The intricate artificial fracture network created by horizontal well fracturing, along with the presence of microcracks in the reservoir, significantly impacts the core imbibition recovery rate [22]. Core experiment results indicate that, at the core scale, fractures enhance the contact area between the imbibition fluid and the rock matrix, potentially increasing the imbibition recovery rate by approximately 10%. Furthermore, the imbibition rate accelerates with the number of fractures [23]. In the process of horizontal well injection–shut-in–production process, imbibition primarily takes place during the injection and shut-in stages. The presence of displacement during the injection stage significantly influences reservoir imbibition. Therefore, understanding the synergistic effects of imbibition and displacement under varying displacement pressure differences is crucial for enhancing imbibition recovery [24]. Wang et al. [25] utilized mathematical models to quantitatively characterize the displacement and imbibition mechanisms in tight oil reservoirs. They clarified the development characteristics of these reservoirs under low pressure conditions, identifying imbibition as the primary mechanism and displacement as the secondary one.

While researchers have elucidated the influence of various factors on imbibition through core experiments and mathematical models, studies focusing on the imbibition mechanism at the pore scale remain limited. In the field of pore-scale simulation, the commonly used numerical methods primarily include the pore network model, the lattice Boltzmann method, the level set method, and the phase field method [26–29]. Among these, the phase field method calculates fluid motion parameters and accurately describes the dynamic evolution of two-phase interfaces within complex pore geometries. This unique advantage makes it particularly well-suited for simulating microscopic two-phase flow in complex porous media [30,31]. Based on the phase field method, Meng et al. [32] simulated counter-current imbibition with varying pore structures. The results indicate that heterogeneous grids demonstrate a better recovery efficiency, and both capillary force and capillary back pressure significantly influence imbibition recovery efficiency. Fracture and reservoir pore wettability are crucial factors influencing imbibition [33]. Wang et al. [34] studied the synergistic effect of imbibition–displacement by combining experimental and simulation methods. Their study found that the imbibition effect becomes more obvious as the fracture density increases. Xia et al. [35] studied the influence of fractures on dynamic imbibition recovery based on fractal theory. The results show that the oil phase imbibition recovery rate increases with the increase in the number of branch fractures. Liu et al. [36] simulated the influence of the complex wettability of pore walls and fracture morphology on imbibition recovery. The study shows that, in complex wettability pores, Y-type fractures have higher recovery rates. Chen et al. [37] found that fracture wettability has a certain influence on imbibition recovery and residual oil distribution.

The laminae in the Santanghu shale oil reservoir are well developed, exhibiting significant wettability differences between layers. Fractures are easily formed during water injection and fracturing processes. To elucidate the imbibition behavior of laminated shale oil reservoirs, based on phase field theory, this study investigates the synergistic effects of displacement and imbibition under varying pressure gradients, as well as the influence of different tortuosity degrees in fractures and wettability discrepancies among the laminae on the imbibition process.

2. Pore-Scale Numerical Simulation

Phase field theory is a method used to describe the evolution of a material's microstructure by distinguishing different phases based on phase field parameters. It employs a diffusion interface model and a free energy functional, allowing for the modeling of phase transitions without the need for precise tracking of the interface. In this study, the COMSOL Multiphysics software was utilized for phase field simulations. The mathematical model and the physical model based on the phase field method are presented below.

2.1. Mathematical Model

In the phase field model, the interface between the two phases is represented as a diffusion interface layer instead of a distinct surface, as illustrated in Figure 1. The blue in the figure represents the water phase, the red represents the oil phase, and the middle of the figure represents the two-phase region. The movement and deformation of this interface are affected by both convection and diffusion.

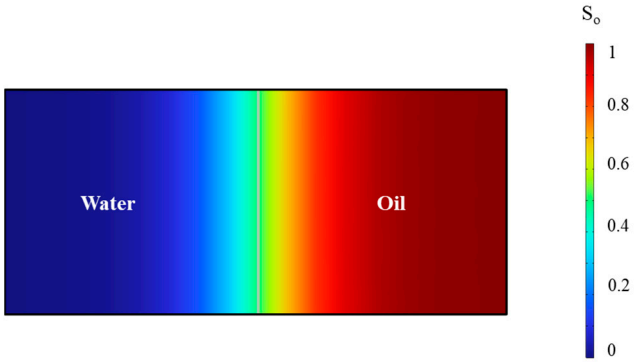


Figure 1. Schematic of the interface diffusion between two phases based on the phase field method.

The dynamic changes in the position of each fluid phase and the interface between the two phases are represented by the phase field parameter ϕ:

$$\phi = \begin{cases} \phi(x,t) = -1 & Fluid\ 1 \\ \phi(x,t) \in (0,1) & Phase\ interface \\ \phi(x,t) = 1 & Fluid\ 2 \end{cases} \quad (1)$$

In phase field theory, the Cahn–Hilliard equation is frequently employed to describe the diffusion at the interface between two phases, as shown below [38]:

$$\frac{\partial \phi}{\partial t} + \boldsymbol{u} \cdot \nabla \phi = \nabla \cdot \gamma \nabla \boldsymbol{G} \quad (2)$$

In COMSOL Multiphysics, this equation is represented as two separate equations:

$$\frac{\partial \phi}{\partial t} + \boldsymbol{u} \cdot \nabla \phi = \nabla \frac{\gamma \lambda}{\varepsilon^2} \nabla \boldsymbol{\psi} \quad (3)$$

$$\boldsymbol{\psi} = -\nabla\varepsilon^2\nabla\phi + \phi\left(\phi^2 - 1\right) \tag{4}$$

where $\boldsymbol{u}$ is the fluid velocity, m/s, γ is the mobility, $m^3 \cdot s/kg$, $\boldsymbol{G}$ is the chemical potential, Pa, and λ is the interfacial free energy density.

The chemical potential is expressed as:

$$\boldsymbol{G} = \lambda\left[-\nabla^2\phi + \frac{\phi(\phi^2 - 1)}{\epsilon^2}\right] \tag{5}$$

The interfacial free energy density is a function of surface tension and interface thickness:

$$\sigma = \frac{2\sqrt{2}}{3}\frac{\lambda}{\varepsilon} \tag{6}$$

In the phase field method, the mobility determines the time scale of the Cahn–Hilliard diffusion and must be large enough to maintain a constant interface thickness, but small enough so that the convection term is not overly damped. The mobility is determined by the mobility adjustment parameter and the interface thickness:

$$\gamma = \chi\varepsilon^2 \tag{7}$$

where χ is the mobility adjustment parameter, m·s/kg, and ε is the interface thickness, m.

Assuming that the oil–water two-phase flow in the pores is an incompressible flow, and ignoring the effects of gravity and inertia, the two-phase flow motion equation can be expressed as [39]:

$$\rho(\boldsymbol{u}\cdot\nabla)\boldsymbol{u} = \nabla\cdot\left[-p\mathbf{I} + \mu\left(\nabla u + \nabla u^T\right)\right] + \boldsymbol{F} \tag{8}$$

where μ is the fluid viscosity, mPa s, ρ is the fluid density, kg/m^3, p is the fluid pressure, Pa, and F is the surface tension acting at the interface. In phase field theory, the surface tension is expressed as:

$$\boldsymbol{F} = \boldsymbol{G}\nabla\phi = \lambda\left[-\nabla^2\phi + \frac{\phi(\phi^2 - 1)}{\epsilon^2}\right]\nabla\phi \tag{9}$$

For the two-phase incompressible flow, the continuity equation can be expressed as:

$$\rho\nabla\cdot\boldsymbol{u} = 0 \tag{10}$$

The volume fractions of oil–water two-phase flow are calculated as:

$$V_{f1} = \frac{1 - \phi}{2} \tag{11}$$

$$V_{f2} = \frac{1 + \phi}{2} \tag{12}$$

where V_{f1} is the volume fraction of fluid 1 and V_{f2} is the volume fraction of fluid 2. In this study, oil is fluid 1 and water is fluid 2.

The density and viscosity of the fluid at the interface between the two phases are shown below:

$$\rho = \rho_1 V_{f1} + \rho_2 V_{f2} \tag{13}$$

$$\mu = \mu_1 V_{f1} + \mu_2 V_{f2} \tag{14}$$

where ρ is the density of the mixed fluid, kg/m^3, μ is the viscosity of the mixed fluid, mPa s, ρ_1 is the density of fluid 1, kg/m^3, ρ_2 is the density of fluid 1, kg/m^3, μ_1 is the viscosity of fluid 1, mPa s, and μ_2 is the viscosity of fluid 2, mPa s.

2.2. Geometry Model and Parameters

The lithology of the Santanghu laminated shale oil reservoir consists of silty dolomite and tuffaceous dolomite. The rock pores are primarily micro-nano pores, with micro-scale pores being the main permeable pores. Therefore, to investigate the synergy effect of displacement–imbibition at the pore scale and the impact of factors such as fractures on imbibition, this study employed the ball packing method to establish a porous media model, as illustrated in Figure 2. The model dimensions were 60 μm in length and 30 μm in width. The white circular simulated rock particles had diameters varying between 0.2 and 2 μm. The model exhibited a porosity of 0.39, with a calculated permeability of 3.8 mD. To enhance the convergence of the computational process, an additional buffer zone was introduced on the left side of the model.

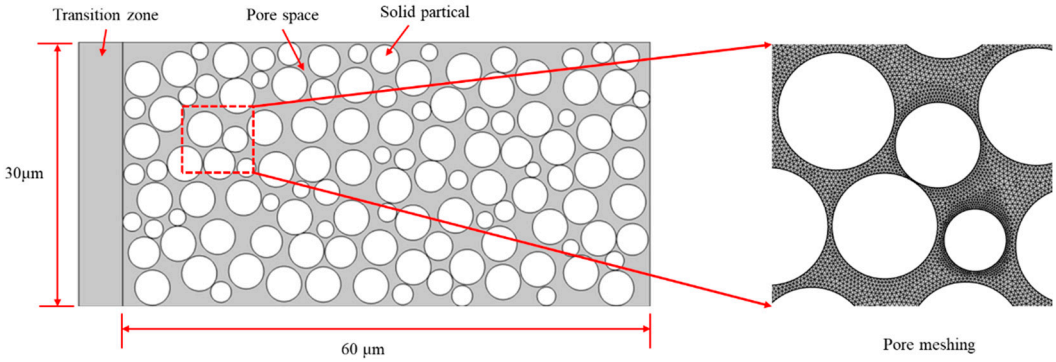


Figure 2. Schematic diagram of the geometric model and the model mesh division.

In order to ensure the convergence of the model, the model grid size was required to be uniform, and the model was meshed using triangular meshes with a size of 0.2 μm. After the model was meshed, it contained 13,289 edge units, 11,787 vertex units, 104,404 triangular meshes, and the average unit quality was 0.8876.

This study assumes that the oil–water mixture is an incompressible fluid, neglecting the influence of gravity on fluid flow during the process. Additionally, the flow was treated as isothermal. In this study, the changes in pore pressure during the injection and shut-in stages were minimal, and, therefore, the impact of pore pressure variations on the imbibition process was neglected. The parameters used in the model simulation are shown in Table 1.

Table 1. The parameters used in the model simulation.

Parameters	Value
Oil density/kg/m^3	850
Oil viscosity/mPa s	3.5
Water density/kg/m^3	1000
Water viscosity/mPa s	1
Interface tension/mN/m	25
Contact angle/°	30
Mobility parameter/m s/kg	1
Interface thickness/μm	$h_{max}/2$

Where h_{max}, in the table, is the maximum cell thickness.

When calculating the permeability of the pore model, a single-phase flow was simulated, and the velocity distribution is shown in Figure 3. The figure demonstrates that the flow velocity in the upper part of the pore model is higher, revealing the presence of a dominant seepage channel.

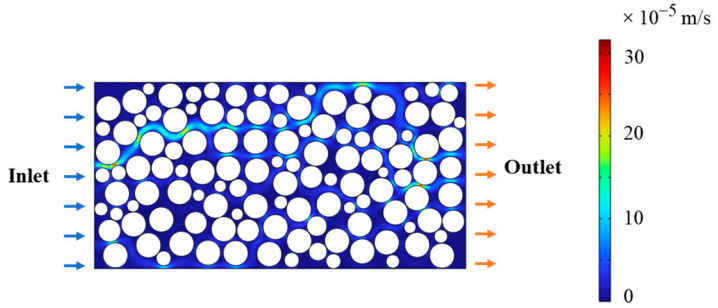


Figure 3. Velocity cloud diagram for the single-phase flow.

3. Results and Discussions

3.1. Oil–Water Distribution Under Different Imbibition Modes

Imbibition can be divided into counter-current imbibition and co-current imbibition according to the direction of the water inflow and the oil outflow. This study simulates the flow of oil and water under various imbibition modes by establishing specific inlet and outlet directions for the fluids. Figure 4 illustrates the oil–water distribution for different imbibition modes, with red representing the oil phase and blue representing the water phase. The blue arrows indicate the direction of the water inflow, while the red arrows show the direction of the oil outflow. The two-phase diffusion interface can be observed intuitively. There are certain differences in the distribution of oil and water under different imbibition modes.

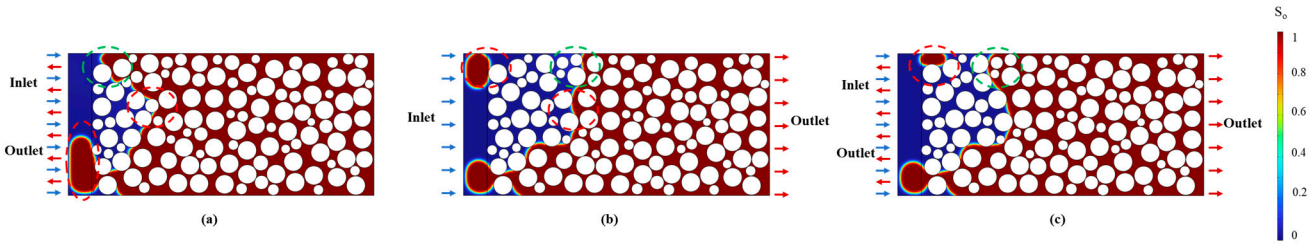


Figure 4. The oil–water distribution for different imbibition modes when t = 10 ms. (**a**) illustrate the counter-current imbibition; (**b**) illustrate the co-current imbibition and (**c**) illustrate the co-current + counter-current imbibition).

Figure 4a shows counter-current imbibition. When counter-current imbibition occurs, water moves along the pores in the middle of the model, and oil is produced from the pores in the lower left corner of the model. Due to the limitation of the transition zone and the viscosity of the oil, the oil droplets continue to gather in the left transition zone to form larger oil droplets. Figure 4b illustrates co-current imbibition. During this process, some oil droplets are expelled from the left transition zone, indicating that counter-current imbibition occurs in co-current imbibition. Water moves along the dominant seepage channel, resulting in an increased sweep range. The oil in the pores above the model is produced under the action of imbibition. Figure 4c shows the oil–water distribution when the co-current imbibition and counter-current imbibition exist at the same time. It can be seen from the figure that the water sweep range is reduced compared with the co-current imbibition. The interface movement distance in the upper part of model is less than that

observed during co-current imbibition, whereas the interface movement distance in the middle of the model increases.

The displacement distance of the front interface and recovery during different imbibition processes are shown in Figure 5. The solid line in the figure represents the recovery rate curve, while the dotted line indicates the movement distance of the front interface. As illustrated in the figure, the co-current imbibition achieves the highest recovery, while the counter-current imbibition yields the lowest recovery. During the initial stage of imbibition, the recovery rate of the counter-current imbibition is higher, and counter-current imbibition is the main imbibition mode. As the imbibition proceeds, the pore recovery rate increases with the increase in the displacement of the front edge of the oil–water interface, with co-current imbibition becoming the primary imbibition mode. Based on the variation in oil–water distribution and the displacement distance of the oil–water interface across different imbibition processes, it can be inferred that co-current imbibition occurs when water advances along the dominant seepage channel, resulting in the production of oil droplets from the surrounding pores. Conversely, the presence of reverse imbibition hinders the progression of water within the dominant seepage channel, ultimately reducing the imbibition rate.

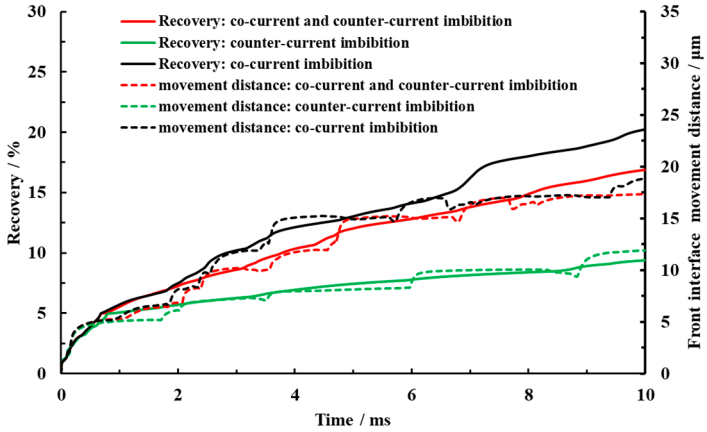


Figure 5. Recovery and oil–water interface front displacement of different imbibition modes.

3.2. Synergistic Effect of Displacement–Imbibition Under Different Pressures

During the injection and shut-in imbibition of water, the flow of fluid in the pores is not entirely static. As the water migrates, both the pressure and the fluid flow rate decrease. In order to clarify the synergistic effect of displacement–imbibition under different pressures, this study set a certain initial velocity at the inlet to study the oil–water distribution and recovery rate during the synergistic oil displacement process. The water flow rates in the study were set to 1 mm/s, 10 mm/s, and 100 mm/s. Due to variations in fluid flow velocities and breakthrough times from the right end, it is not possible to effectively analyze the fluid and pressure distributions at the same time. Therefore, this study examines the oil–water and pressure distributions under the same injection volume, as shown in Figure 6.

Figure 6a,b illustrate the oil–water and pressure distributions at an injection speed of 1 mm/s, respectively. Figure 6c,d present these distributions at 10 mm/s, while Figure 6e,f depict them at 100 mm/s. The figure shows that, at a water injection speed of 1 mm/s, the pressure gradient is 41.6 Pa/μm. The direction of the oil–water interface tension aligns with the injection direction. The pressure at the oil–water interface is higher. This indicates that capillary force acts as the driving force, and the imbibition effect, driven by capillary action, is the primary method of oil displacement. At a water drive speed of 10 mm/s, the pressure gradient is 750 Pa/μm, with pressure distributed along the flooding direction. As the water injection speed increases, the curvature of the oil–water interface decreases. In this scenario,

the capillary force and displacement force offset each other, resulting in a diminished synergistic oil recovery effect. At a water drive speed of 100 mm/s, the pressure gradient reaches 7300 Pa/μm. At this speed, the direction of the oil–water interfacial tension opposes the water injection direction, resulting in capillary force acting as displacement resistance. This results in the formation of a distinct two-phase region during the displacement process, leading to a low washing efficiency.

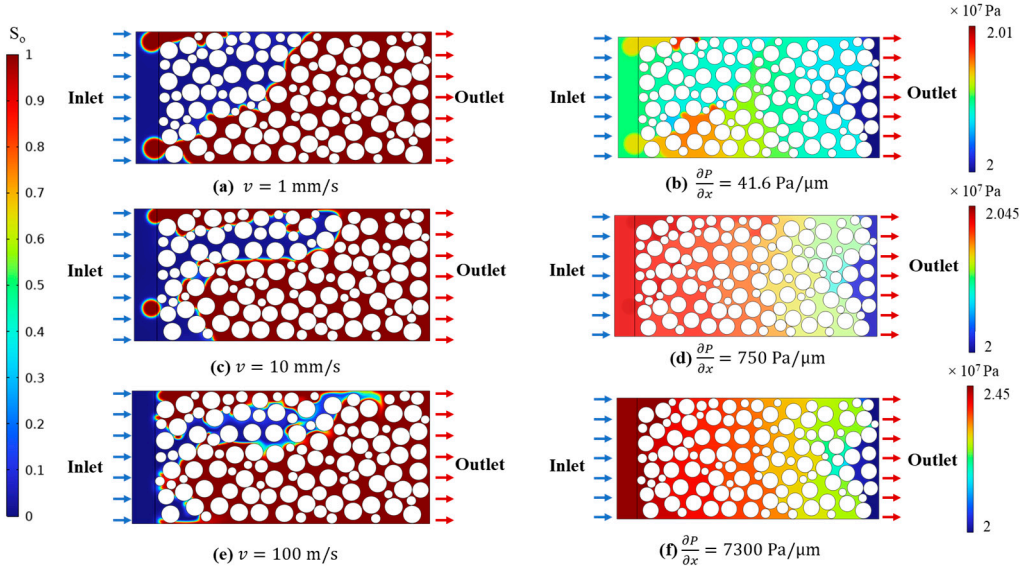


Figure 6. Oil–water distribution and pressure distribution at different injection rates. (**a**,**c**,**e**) illustrate the oil–water distribution when injecting 0.2 PV at an injection speeds of 1 mm/s, 10 mm/s, and 100 mm/s, respectively; (**b**,**d**,**f**) illustrate the pressure distribution when injecting 0.2 PV at an injection speeds of 1 mm/s, 10 mm/s, and 100 mm/s, respectively.

The movement distance of the oil–water interface front and the recovery rate at different injection rates are shown in Figure 7. Before the water breaks through from the right end, the pore recovery increases continuously with the movement distance of the front interface. When the injection speed is 1 mm/s, under the synergistic effect of displacement–imbibition, the water sweep range and the oil washing efficiency are high, resulting in the highest recovery. Although the interface front displaces at its fastest at 100 mm/s, the pore recovery rate is the lowest due to the water fingering phenomenon and the reduced oil washing efficiency. By comparing the front interface moving distance and pore recovery rate under different pressures, it can be found that lower water injection rates result in a later breakthrough time and a higher recovery rate at the moment of water breakthrough. Additionally, as shown in Figure 7, the recovery curves for injection speeds of 10 mm/s and 100 mm/s differ from the curve for 1 mm/s. At higher injection speeds, water breaks through from the right end without surrounding the oil in the pores, allowing the movable oil to be extracted through displacement. As the injection speed increases, the recovery rate also increases. However, at lower injection speeds, once water breaks through from the right end, it surrounds the fluid in the pores, creating a capillary effect. This additional resistance prevents the effective production of oil from the pores.

The imbibition during the shut-in stage significantly affects the pore recovery rate. This study simulates the imbibition after the injection of water by controlling the flow rate at the inlet end. Additionally, by varying the injection times, the impact of water saturation on imbibition after water injection is examined. Based on the above research, the fluid injection speed is 1 mm/s, and the injection time is 5 ms and 10 ms, respectively. The recovery rate with different injection times is shown in Figure 8. Figure 8a, 8b show the

recovery factors when injection is 5 ms and 10 ms, respectively. The red dashed circle in the figure is the imbibition-produced fluid, and the green dashed circle indicates the secondary-injection-produced fluid.

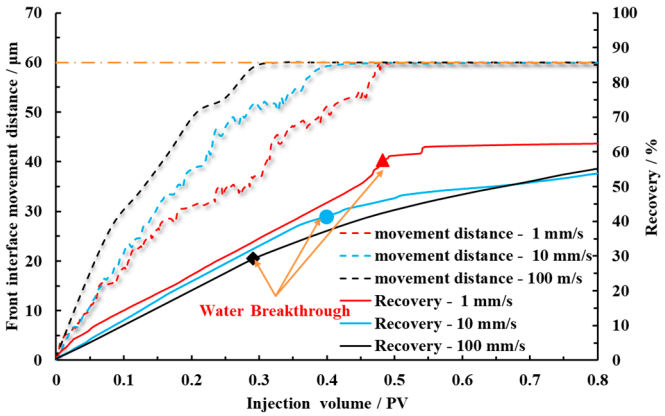


Figure 7. The movement distance of the oil–water interface front and the recovery rate at different injection rates.

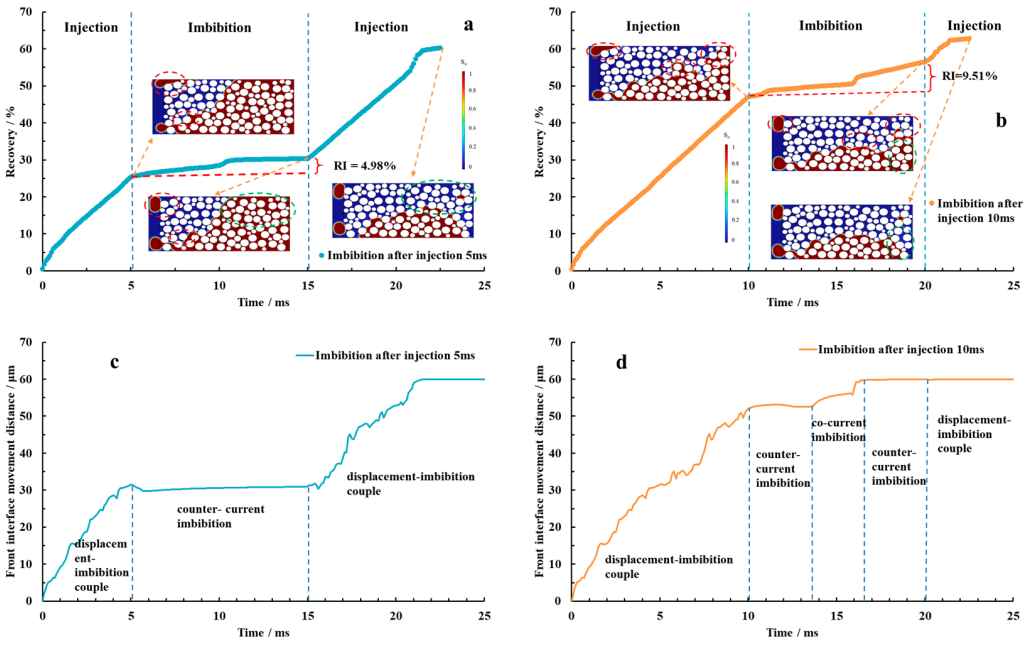


Figure 8. The recovery rate and front interface movement distance with different injection time. ((**a**,**b**) illustrate the recovery and the oil-water distribution when injection for 5 ms and 10 ms, respectively; (**c**,**d**) illustrate the front interface movement distance during processes the injection and imbibition when injection for 5 ms and 10 ms, respectively).

In the injection stage, the oil recovery rate of displacement–imbibition synergistic flooding increases with injection time. In the shut-in stage, the injection rate at the inlet is 0, the fluid in the pores is only produced under the action of imbibition, and the recovery rate increases slowly. The imbibition mode during the imbibition process can be inferred from the recovery rate and the movement distance of the oil–water interface front, as illustrated in Figure 8c,d. In the co-current imbibition stage, the oil recovery rate increases as the oil–water interface front advances. In the counter-current imbibition stage, the oil–water front interface remains almost unchanged and the oil recovery rate increases.

By comparing the imbibition effects after varying injection times, it can be inferred that an increase in the oil–water contact area effectively enhances the water imbibition process. Additionally, the rise in water saturation amplifies the co-current water imbibition

effect. Compared to injecting for 5 ms, injecting for 10 ms results in a 4.53% increase in imbibition recovery during the shut-in stage. After imbibition, a high oil saturation allows for the continued water flooding to enhance the recovery. Once water breakthrough occurs at the right end, the residual oil becomes surrounded by water, preventing the effective recovery through additional flooding. The remaining oil after flooding is predominantly located in the low-permeability zones in the middle of the model. Oil droplets at the pore boundaries are recovered due to the imbibition process.

3.3. Effect of Fracture Tortuosity on Imbibition

Microcracks commonly form in shale oil reservoirs, enhancing pore connectivity and creating high-speed seepage channels for fluids. Fracture tortuosity is defined as the ratio of the actual length of the fracture to the apparent length of the seepage medium, reflecting the complexity of fluid flow pathways:

$$\tau = \frac{L_t}{L_0} \tag{15}$$

where τ is the fracture tortuosity, dimensionless, L_t is the actual length of the fracture, μm, and L_0 is the apparent length of the seepage medium, μm.

As a critical parameter of fractures, fracture tortuosity significantly influences imbibition recovery. In this study, fractures with different tortuosity degrees were constructed within the model to examine their effect on imbibition. The recovery associated with different degrees of fracture tortuosity is illustrated in Figure 9. In Figure 9, the tortuosity of fractures 1 to 3 increases gradually, while fracture 4 exhibits the same level of tortuosity as fracture 3, albeit in the opposite direction. The blue arrow in the figure indicates the direction of fluid flow.

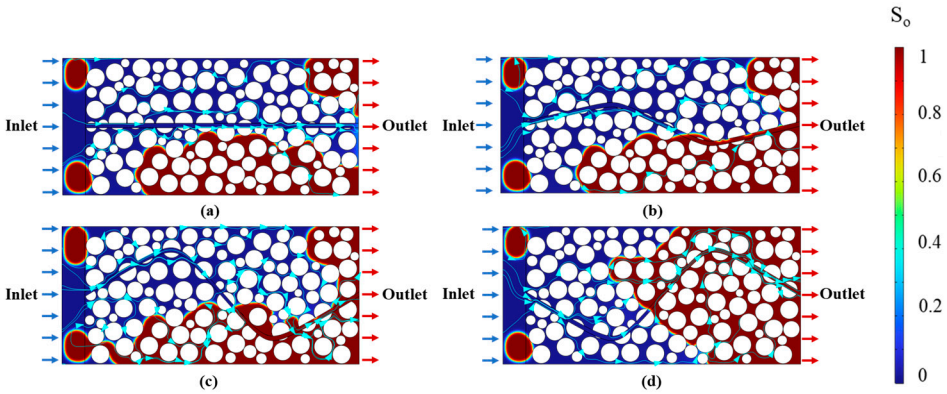


Figure 9. Oil–water distribution during imbibition with different degrees of fracture tortuosity. (**a**) illustrate the oil-water distribution of Fracture 1 (τ = 1); (**b**) illustrate the oil-water distribution of Fracture 2 (τ = 1.04); (**c**) illustrate the oil-water distribution of Fracture 3 (τ = 1.21); (**d**) illustrate the oil-water distribution of Fracture 4 (τ = 1.21)).

Figure 9 clearly demonstrates that the presence of fractures enhances the pore sweep efficiency. As fracture tortuosity increases, the advancement of the oil–water interface slows, resulting in a decreased imbibition rate. The streamline diagram indicates that, during the imbibition process, oil and water preferentially flow along the fractures and the high-permeability pathways within the pores. Both the direction and the fracture tortuosity have a substantial impact on the imbibition recovery rate and the distribution of residual oil. It can be seen from Figure 9a–c that, as fracture tortuosity increases, the overlap between the fractures and the high-permeability zones in the pores also increases. Consequently, the crude oil is extracted from these zones. Oil–water distribution over time as shown in Figure 10. The blue arrow in the figure indicates the direction of fluid flow. Over time,

water progressively infiltrates the pores through the high-permeability zones, displacing crude oil from the pore spaces. The fracture tortuosity directions in Figure 9c,d are opposite. Figure 9d shows that the crude oil in the low-permeability area near the fracture becomes effectively mobilized. However, the displacement velocity of the oil–water interface front is low. The pore recovery rate and the front interface movement distance under different tortuosity conditions are shown in Figure 11. The figure indicates that the movement distance of the oil–water interface front for fracture 3 is the fastest before 10 ms. This rapid movement is attributed to the overlap between the fracture and the high-speed seepage channel in the pores. The second half of fracture 3 is located near the low-permeability area of the pore, such an area increasing the water sweep scope and also reducing the displacement speed of the oil–water front interface. Although the oil–water front interface of fracture 4 moves slowly, the oil in the low-permeability pores is effectively mobilized due to the fracture's location, resulting in a relatively high recovery rate. When the imbibition time is 20 ms, the movement distance of the oil–water interface front edge in fracture 4 is 35 μm, accounting for only 58% of that of fracture 1, but their recovery rates are all around 60%.

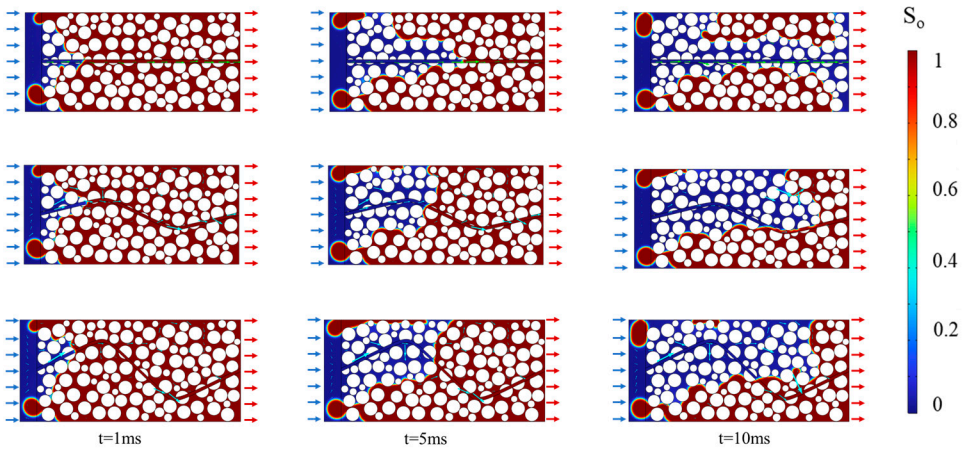


Figure 10. Oil–water distribution with varying degrees of fracture tortuosity over time.

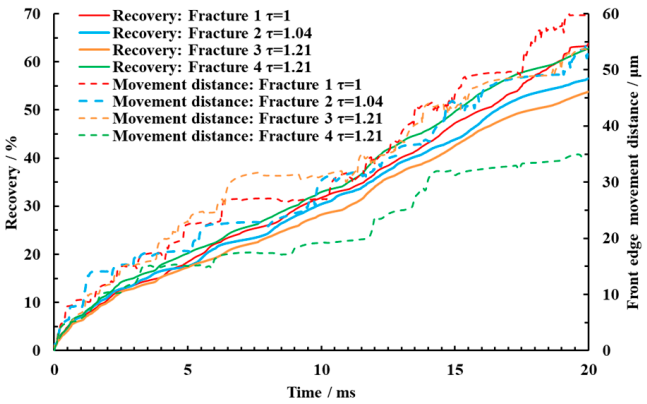


Figure 11. The movement distance of the oil–water interface front and the recovery rate with different fractures.

3.4. Effect of Laminal Wettability Differences on Imbibition

Considering the presence of fractures in shale oil reservoirs and the differences in pore wettability on either side of the fractures, a model was developed to simulate the microscopic imbibition characteristics of laminated shale oil reservoirs, as illustrated in Figure 12. The contact angle of the pores above the fracture is 30°, while the contact angle

of the pores below the fracture is 60°. In combination with the above research, the flow rate at the inlet was set to 1 mm/s, and spontaneous imbibition was performed after 10 ms.

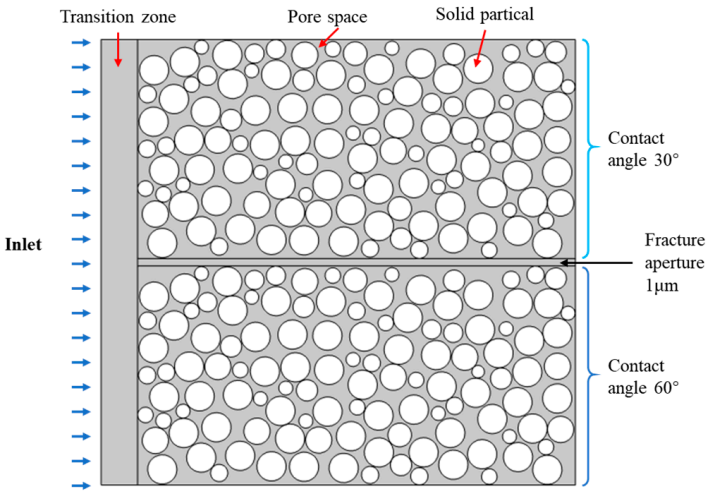


Figure 12. The model considering laminal fractures and the differences in pore wettability on either side of the fractures.

The pore recovery rate of different areas is shown in Figure 13. The figure demonstrates that wettability significantly influences the pore recovery factor. The stronger the pore water wettability, the higher the oil displacement efficiency. The distribution of oil–water during the oil displacement process is shown in Figure 14. The blue arrow in the figure indicates the direction of fluid flow. During the injection stage, the fluid migrates rapidly along the fracture and breaks through the right end of the pore at 8.1 ms. The oil in the strongly water-wet pores is produced first. During the static imbibition period, the fluid near the right end boundary of the pore is produced under the action of imbibition, and the residual oil is surrounded by water. The oil recovery rate of the weakly water-wet pores is poor, and only the pores at the inlet and around the fractures are produced. The wettability difference around laminal fractures causes the water to finger in the strongly wetted area, and the oil in the weakly water-wetted area is difficult to mobilize. The recovery rate in the strongly wetted area (contact angle 30°) is 35% higher than that in the weakly water-wetted area (contact angle 60°). Chen et al. [37] also found in their research that, as the wettability increases, the imbibition recovery rate improves. Therefore, for laminated shale oil reservoirs with large wettability differences, surfactants should be used to improve the wettability of the weakly water-wetted area and reduce the fingering phenomenon, thereby enhancing the pore recovery rate.

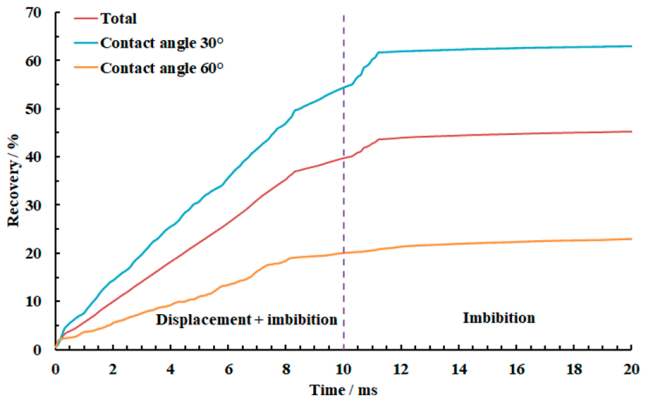


Figure 13. The pore recovery rate of different areas.

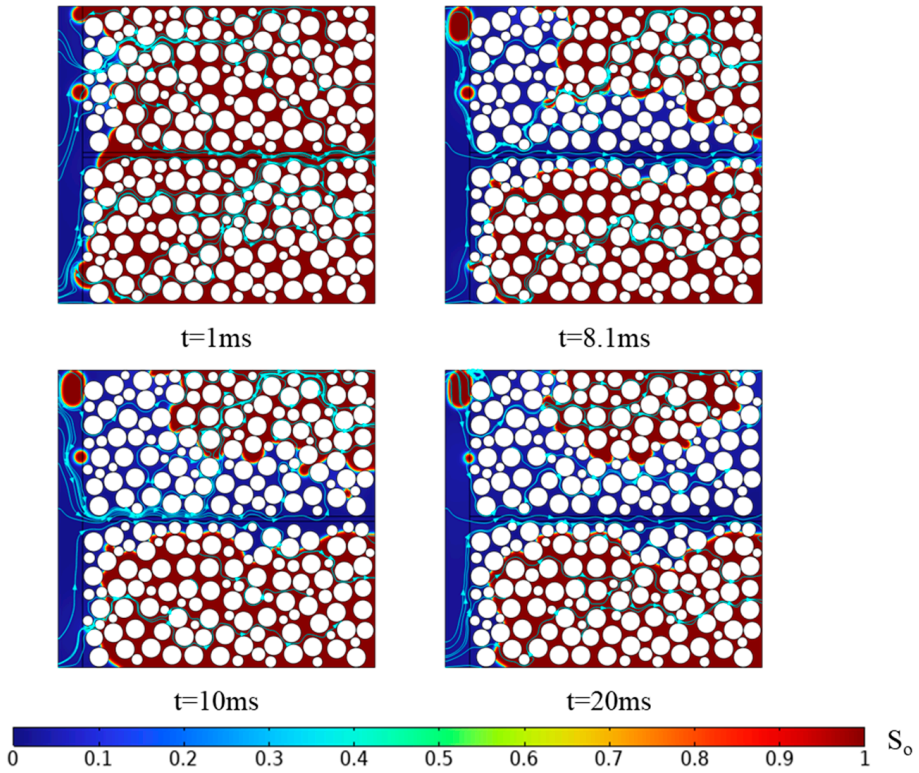


Figure 14. The distribution of oil–water during the oil displacement process.

4. Conclusions

This study simulates the oil–water distribution during the imbibition process based on the phase field method. The effects of the displacement–imbibition synergy, fracture tortuosity, and wettability differences on imbibition are studied, and the following conclusions are drawn:

1. Different imbibition modes result in distinct differences in pore recovery: co-current imbibition > co-current imbibition + counter-current imbibition > counter-current imbibition. Co-current imbibition predominantly occurs in the dominant seepage channels, while counter-current imbibition mainly takes place in pore boundary regions, inhibiting the advancement of water in the dominant seepage channels, leading to a wider water distribution but a reduced overall imbibition rate.
2. During the water injection stage, a low injection rate is beneficial for synergistic oil recovery through imbibition and displacement. As the injection rate increases, the capillary imbibition effect diminishes. There is a fingering phenomenon when the injection rate exceeds 10 mm/s. At injection rates above 100 mm/s, capillary forces act as resistance to oil displacement, creating a two-phase flow regime within the pores. The rise in water saturation amplifies the co-current water imbibition effect. Compared to injecting for 5 ms, injecting for 10 ms results in a 4.53% increase in imbibition recovery during the shut-in stage.
3. The water sweep efficiency increases with the tortuosity of the fractures. Fractures in high-permeability zones accelerate the movement of the oil–water interface, while fractures in low-permeability zones enhance water sweep efficiency in the low-permeability regions.
4. The wettability difference across fractures cause water to penetrate along the strongly water-wet pores, while only the inlet end and the pores near the fracture in the weakly water-wet zone are affected. The recovery rate in the strongly wetted area (contact angle 30°) is 35% higher than that in the weakly water-wetted area (contact angle 60°).

Surfactants should be used to improve the wettability of the weakly water-wetted area and reduce the fingering phenomenon, thereby enhancing the pore recovery rate.

Author Contributions: Conceptualization, K.Y. and S.Y.; methodology, K.Y.; formal analysis, X.L.; writing—original draft preparation, K.Y.; writing—review and editing, S.Z. and J.K.; funding acquisition, S.Y. All authors have read and agreed to the published version of the manuscript.

Funding: This study was supported by the National Key Basic Research and Development Program (2023YFB4104204) and the National Natural Science Foundation of China (U23B2090).

Data Availability Statement: The raw data supporting the conclusions of this article will be made available by the authors on request.

Conflicts of Interest: Jilun Kang was employed by Research Institute of Exploration and Development, Tuha Oilfield Company, Petro China. The remaining authors declare that the research was conducted in the absence of any commercial or financial relationships that could be construed as a potential conflict of interest.

References

1. Zou, C.; Yang, Z.; Cui, J.; Zhu, R.; Hou, L.; Tao, S.; Yuan, X.; Wu, S.; Lin, S.; Wang, L.; et al. Formation mechanism, geological characteristics and development strategy of nonmarine shale oil in China. *Pet. Explor. Dev.* **2013**, *40*, 14–26. [CrossRef]
2. Hu, S.; Zhao, W.; Hou, L.; Yang, Z.; Zhu, R.; Wu, S.; Bai, B.; Jin, X. Development potential and technical strategy of continental shale oil in China. *Pet. Explor. Dev.* **2020**, *47*, 877–887. [CrossRef]
3. Taheri-Shakib, J.; Kantzas, A. A comprehensive review of microwave application on the oil shale: Prospects for shale oil production. *Fuel* **2021**, *305*, 121519. [CrossRef]
4. Wang, Z.; Zhang, T.; Liu, S.; Ding, K.; Liu, T.; Yao, J.; Sun, H.; Yang, Y.; Zhang, L.; Wang, W.; et al. Unveiling nanoscale fluid miscible behaviors with nanofluidic slim-tube. *Energy Environ. Sci.* **2024**, *17*, 9635. [CrossRef]
5. Wang, D.; Butler, R.; Liu, H.; Ahmed, S. Flow-Rate Behavior and Imbibition in Shale. *SPE Reserv. Eval. Eng. Reserv. Eval. Eng.* **2011**, *14*, 505–512. [CrossRef]
6. Zhou, Z.; Abass, H.; Li, X.; Bearinger, D.; Frank, W. Mechanisms of imbibition during hydraulic fracturing in shale formations. *J. Pet. Sci. Eng.* **2016**, *141*, 125–132. [CrossRef]
7. Li, Q.; Li, Q.; Cao, H.; Wu, J.; Wang, F.; Wang, Y. The Crack Propagation Behaviour of CO_2 Fracturing Fluid in Unconventional Low Permeability Reservoirs: Factor Analysis and Mechanism Revelation. *Processes* **2025**, *13*, 159. [CrossRef]
8. Li, Q.; Li, Q.; Wu, J.; Li, X.; Li, H.; Cheng, Y. Wellhead Stability During Development Process of Hydrate Reservoir in the Northern South China Sea: Evolution and Mechanism. *Processes* **2025**, *13*, 40. [CrossRef]
9. Peng, X.; Wang, X.; Zhou, X.; Lin, Z.; Zeng, F.; Huang, X. Lab-on-a-chip systems in imbibition processes: A review and applications/issues for studying tight formations. *Fuel* **2021**, *306*, 121603. [CrossRef]
10. Liu, Q.; Song, R.; Liu, J.; Lei, Y.; Zhu, X. Pore-scale visualization and quantitative analysis of the spontaneous imbibition based on experiments and micro-CT technology in low-permeability mixed-wettability rock. *Energy Sci. Eng.* **2020**, *8*, 1840–1856. [CrossRef]
11. Suo, S.; Liu, M.; Gan, Y. Modelling Imbibition Processes in Heterogeneous Porous Media. *Transp. Porous Media* **2019**, *126*, 615–631. [CrossRef]
12. Handy, L.L. Determination of Effective Capillary Pressures for Porous Media from Imbibition Data. *Trans. AIME* **1960**, *219*, 75–80. [CrossRef]
13. Ning, X.; Ewing, R.; Hu, Q.; Wang, Q.; Zhang, X. A New Model for Simulating the Imbibition of a Wetting-Phase Fluid in a Matrix-Fracture Dual Connectivity System. *Geofluids* **2022**, *2022*, 7408123. [CrossRef]
14. Wang, F.; Zhao, J. Mathematical model of liquid spontaneous imbibition into gas-saturated porous media with dynamic contact angle and gravity. *Chem. Eng. Sci.* **2021**, *229*, 116139. [CrossRef]
15. Guo, J.; Li, M.; Chen, C.; Tao, L.; Liu, Z.; Zhou, D. Experimental investigation of spontaneous imbibition in tight sandstone reservoirs. *J. Pet. Sci. Eng.* **2020**, *193*, 107395. [CrossRef]
16. Xu, D.; Bai, B.; Wu, H.; Hou, J.; Meng, Z.; Sun, R.; Li, Z.; Lu, Y.; Kang, W. Mechanisms of imbibition enhanced oil recovery in low permeability reservoirs: Effect of IFT reduction and wettability alteration. *Fuel* **2019**, *244*, 110–119. [CrossRef]
17. Dai, C.; Cheng, R.; Sun, X.; Liu, Y.; Zhou, H.; Wu, Y.; You, Q.; Zhang, Y.; Sun, Y. Oil migration in nanometer to micrometer sized pores of tight oil sandstone during dynamic surfactant imbibition with online NMR. *Fuel* **2019**, *245*, 544–553. [CrossRef]
18. Qingbang Meng, H.L.J.W. Effect of Fluid Viscosity on Correlation of Oil Recovery by Linear Counter-Current Spontaneous Imbibition. *J. Pet. Sci. Eng.* **2017**, *151*, 341–347. [CrossRef]

19. Cheng, Z.; Ning, Z.; Yu, X.; Wang, Q.; Zhang, W. New insights into spontaneous imbibition in tight oil sandstones with NMR. *J. Pet. Sci. Eng.* **2019**, *179*, 455–464. [CrossRef]
20. Cai, J.; Yu, B.; Zou, M.; Luo, L. Fractal Characterization of Spontaneous Co-current Imbibition in Porous Media. *Energy Fuels* **2010**, *24*, 1860–1867. [CrossRef]
21. Jing, W.; Huiqing, L.; Genbao, Q.; Yongcan, P.; Yang, G. Investigations on spontaneous imbibition and the influencing factors in tight oil reservoirs. *Fuel* **2019**, *236*, 755–768. [CrossRef]
22. Cheng, H.; Wang, F. Mathematical model of the spontaneous imbibition of water into oil-saturated fractured porous media with gravity. *Chem. Eng. Sci.* **2021**, *231*, 116317. [CrossRef]
23. Yang, K.; Wang, F.; Zhao, J. Experimental study of surfactant-enhanced spontaneous imbibition in fractured tight sandstone reservoirs: The effect of fracture distribution. *Pet. Sci.* **2023**, *20*, 370–381. [CrossRef]
24. Pi, Z.; Peng, H.; Jia, Z.; Zhou, J.; Cao, R. Coupling mechanisms of displacement and imbibition in pore-fracture system of tight oil reservoir. *Capillarity* **2023**, *7*, 13–24. [CrossRef]
25. Wang, F.; Zeng, F.; Zhao, J. A mathematical model of displacement and imbibition of lowpermeability/ tight reservoirs and its application]. *Acta Pet. Sin.* **2020**, *41*, 1396–1405.
26. Liu, Y.; Zhu, R.; Yu, P.; Wang, J.; Zhao, J. Counter-current spontaneous imbibition dynamics: Combined effects of wettability, fracture flow, and pore structure. *Phys. Fluids* **2024**, *36*, 032131. [CrossRef]
27. Qin, C.; van Brummelen, H.; Hefny, M.; Zhao, J. Image-based modeling of spontaneous imbibition in porous media by a dynamic pore network model. *Adv. Water Resour.* **2021**, *152*, 103932. [CrossRef]
28. Liu, H.; Sun, S.; Wu, R.; Wei, B.; Hou, J. Pore-Scale Modeling of Spontaneous Imbibition in Porous Media Using the Lattice Boltzmann Method. *Water Resour. Res.* **2021**, *57*, e2020WR029219. [CrossRef]
29. Gao, X.; Yang, S.; Wang, B.; Zhanga, Y.; Hu, J.; Wang, M.; Shen, B.; Zhao, E. Pore-scale modeling of multiple fluids flow transport kinetics for CO_2 enhanced gas recovery. *Energy* **2025**, *315*, 134486. [CrossRef]
30. Wang, D.; Ma, Y.; Song, K.; Tao, J.; Bao, R.; Zhang, J. Phase-Field Modeling of Pore-Scale Oil Replacement by Spontaneous Imbibition in Fractured Porous Media. *Energy Fuels* **2022**, *36*, 14824–14837. [CrossRef]
31. Yang, L.; Li, M.; Zhang, H.; Liu, Y.; Liu, Z.; Zhang, Z.; Gong, F.; Wang, S. Phase-Field Simulation of Counter-Current Imbibition and Factors Influencing Recovery Efficiency. In *Transport in Porous Media*; Springer Nature: Berlin/Heidelberg, Germany, 2024.
32. Meng, Q.; Zhao, L.; Li, P.; Yang, F.; Cai, J. Experiments and phase-field simulation of counter-current imbibition in porous media with different pore structure. *J. Hydrol.* **2022**, *2022*, 127670. [CrossRef]
33. He, Z.; Liang, F.; Meng, J. Pore-scale study of the effect of bifurcated fracture on spontaneous imbibition in heterogeneous porous media. *Phys. Fluids* **2022**, *34*, 072003. [CrossRef]
34. Wang, B.; Cao, R.; Pi, Z.; Cheng, L.; Jia, Z.; Hu, J. Displacement-imbibition coupling mechanisms between matrix and complex fracture during injecting-shut in-production process using pore-scale simulation and NMR experiment. *Geoenergy Sci. Eng.* **2024**, *242*, 213254. [CrossRef]
35. Xia, D.; Liao, Z.; Wu, M.; Yang, Z.; Li, H.; Shi, D. Quantitative characterization of imbibition in fractured porous media based on fractal theory. *Phys. Fluids* **2024**, *36*, 052115. [CrossRef]
36. Liu, Q.; Li, J.; Liang, B.; Liu, J.; Sun, W.; He, J.; Lei, Y. Complex wettability behavior triggering mechanism on imbibition: A model construction and comparative study based on analysis at multiple scales. *Energy* **2023**, *275*, 127434. [CrossRef]
37. Chen, J.; Yang, Y.; Cao, X.; Zhang, S.; Lv, Q.; Jiang, L.; Cheng, Z.; Liu, Z.; Song, Y.; Li, T. Simulation Study on the Spontaneous Imbibition Mechanism and Influencing Factors of Laminated Shale Oil Reservoirs in Jiyang Depression, Eastern China. *Energy Fuels* **2023**, *37*, 13048–13064. [CrossRef]
38. Badalassi, V.E.; Ceniceros, H.D.; Banerjee, S. Computation of multiphase systems with phase field models. *J. Comput. Phys.* **2003**, *190*, 371–397. [CrossRef]
39. Jacqmin, D. Calculation of Two-Phase Navier—Stokes Flows Using Phase-Field Modeling. *J. Comput. Phys.* **1999**, *155*, 96–127. [CrossRef]

Disclaimer/Publisher's Note: The statements, opinions and data contained in all publications are solely those of the individual author(s) and contributor(s) and not of MDPI and/or the editor(s). MDPI and/or the editor(s) disclaim responsibility for any injury to people or property resulting from any ideas, methods, instructions or products referred to in the content.